Available online at www.sciencedirect.com
ScienceDirect
International Journal of Heat and Fluid Flow 28 (2007) 1098–1111
International Journal of HEAT AND FLUID FLOW
www.elsevier.com/locate/ijhff

Analysis of turbulent flow in channels roughened by two-dimensional ribs and three-dimensional blocks. Part I: Resistance

D.N. Ryu [a], D.H. Choi [a,*], V.C. Patel [b]

[a] Department of Mechanical Engineering, Korea Advanced Institute of Science and Technology, Daejeon 305-701, Republic of Korea
[b] IIHR – Hydroscience and Engineering, Department of Mechanical and Industrial Engineering, The University of Iowa, Iowa City, IA 52242, USA

Received 12 May 2005; received in revised form 21 September 2006; accepted 30 November 2006
Available online 15 February 2007

Abstract

The characteristics of a turbulent flow in channels with two-dimensional ribs and three-dimensional blocks are investigated in the context of surface roughness effects. Reynolds-averaged Navier–Stokes equations, coupled with the k–ω turbulence model with near-wall treatment, are solved by a finite-volume method. Calculations are carried out for ribs with square, triangular, semicircular and wavy cross-sections over a range of rib spacing (pitch) and Reynolds numbers. The pitch that yields maximum resistance is identified for each roughness. For all cases, the space-averaged velocity profile exhibits a logarithmic region, with a roughness function that varies logarithmically with the roughness Reynolds number. The roughness function depends on the rib shape and pitch ratio but is independent of the absolute rib size. Analysis with three-dimensional blocks reveals similar but more complex behavior. A logarithmic region exists in the velocity profile but with much smaller block heights compared to ribs. The different block arrangements exhibit quite distinct flow characteristics but the differences tend to vanish as the block height decreases. In general, a Reynolds-averaged numerical model successfully describes the principal features of wall roughness that have hitherto fore been the purview of experimental correlations. *Part II* of the paper extends the model to study heat transfer from a rough surface.

Keywords: Distributed roughness; Similarity law; Roughness function; RANS equations; k–ω model

1. Introduction

Turbulent flow over surfaces roughened by simple geometric elements, such as two-dimensional spanwise ribs or discrete three-dimensional protuberances, continue to be of interest in fluids engineering from several perspectives (Schlichting, 1979). Regular roughness elements are routinely used for heat transfer enhancement (Webb et al., 1971; Sparrow and Tao, 1983). They are also used to study surface roughness effects, in general, as they are easily reproduced in the laboratory and modeled in numerical experiments. Measurements on ribbed surfaces, for example, have provided considerable insight into the mechanisms by which surface roughness effects are felt in the interior of the flow. Of particular concern in practical engineering applications is the existence of similarity laws, principal among which is the logarithmic velocity distribution, upon which friction factor and heat transfer correlations are based.

At sufficiently large distance from the roughness elements, the effect of the individual elements vanishes and the net effect on the velocity profile is felt as reduction in the constant B in the logarithmic law. This change in the constant, B, known as the *roughness function*, depends not only on the roughness size but also on its geometry (Schlichting, 1979). In the case of ribs, for example, the roughness function depends on their shape and pitch (spacing between adjacent ribs). Numerous attempts have been

* Corresponding author. Tel.: +82 42 869 3018; fax: +82 42 869 3210.
E-mail address: d-h-choi@kaist.ac.kr (D.H. Choi).

0142-727X/$ - see front matter © 2007 Elsevier Inc. All rights reserved.
doi:10.1016/j.ijheatfluidflow.2006.11.006

Nomenclature

b, c	length (streamwise) and width (spanwise) of roughness block, Fig. 10
ΔB	roughness function, downward shift in the logarithmic velocity profile
C_p	pressure coefficient $\left(=\frac{p-p_{ref}}{\frac{1}{2}\rho U_b^2}\right)$
d	spanwise spacing of blocks, Fig. 10
D_e	hydraulic diameter, $2H$
f	Darcy friction factor $\left(=\frac{8\tau_x}{\rho \overline{U}^2}\right)$
H	channel height
h	rib height
h^+	roughness Reynolds number $\left(=\frac{hu_\tau}{\nu}\right)$
k	turbulence kinetic energy $(=\overline{u_i u_i}/2)$
p_{ref}	reference pressure, the pressure on top of rib, Eq. (6)
$\hat{p}$	normalized pressure $\left(=\frac{p-p_{ref}}{\rho U_b^2}\right)$
R^+	roughness correlation, Eq. (9)
Re_δ, Re_{D_e}	Reynolds number $\left(=\frac{\bar{U}\delta}{\nu}\right.$ or $\left.\frac{U_b D_e}{\nu}\right)$
$\overline{U}$	average velocity between wall and the point of velocity maximum
U_b	bulk velocity
U_l	space-averaged streamwise velocity
u_τ	space-averaged friction velocity $\left(=\sqrt{\tau_x/\rho}\right)$
u^+	non-dimensional velocity $(=U_l/u_\tau)$
w	rib or block pitch, Figs. 1 and 10
x, y, z	streamwise, normal, and spanwise coordinates, Figs. 1 and 10
y^+	non-dimensional normal distance $(=\frac{yu_\tau}{\nu})$
y_0	location of zero space-averaged velocity, virtual origin

Greek symbols

δ	distance from wall to the point of velocity maximum
ν, ν_t	kinematic viscosity, eddy viscosity
ρ	density
ω	specific dissipation rate
τ_w	local wall shear stress $\left(=\mu\frac{\partial u}{\partial y}\Big\vert_w\right)$
τ_x	space-averaged wall shear stress, Eq. (6)

made to correlate the effects of different types of roughness with the classical experiments of Nikuradse (1950) on sand-grain roughness.

Dvorak (1969) summarized the previous work on rib roughness and proposed a relation between the rib pitch and the roughness function. Perry et al. (1969) experimentally obtained the roughness function for a boundary layer developing on a surface with distributed ribs. They were the first to make the distinction between the so-called *d*- and *k*-type roughness depending on whether the dominant parameter is the boundary-layer thickness (or pipe diameter, *d*) or the rib height (*k*). Since then a number of experimental studies (Jimenez, 2004) have been conducted to better understand the details of the flow over ribbed surfaces.

More recently, advances in turbulence modeling have led to studies of rib roughness using different numerical methods. For example, Cui et al. (2003a,b) used large-eddy simulations (LES) to compute the flow in a two-dimensional channel with ribs with various pitch to height ratios. They showed that a logarithmic layer exists in the space-averaged velocity distribution some distance above the ribs. They also identified the location of the so-called virtual origin with the position of zero space-averaged velocity. Similar studies are reported by Miyake et al. (2002) and Ikeda and Durbin (2002) using direct numerical simulation (DNS).

The importance of similarity laws in engineering correlations of friction and heat transfer mentioned above, and the success of these recent numerical studies suggest that a more comprehensive numerical investigation would yield useful insights into the effects of discrete roughness elements on these parameters. As neither LES nor DNS are cost effective for such purposes, here we use a numerical model based on the Reynolds-averaged Navier–Stokes (RANS) equations and an established two-equation turbulence model to study the effect of different types of discrete roughness on the velocity profile and related correlations. In particular, the existence of a logarithmic layer is examined and the relevant parameters are identified. Although the RANS approach is not suitable for capturing the flow unsteadiness due to large-eddy motions, it is quite adequate for the present study in which only the mean quantities, both in time and space, are of interest. Calculations are carried out for two-dimensional ribs as well as three-dimensional roughness elements. A brief description of the numerical model is presented as the various components are quite well established, and a simple validation study is performed before describing the principal results.

2. Numerical model and validation

2.1. Governing equations

For steady incompressible turbulent flow, the Reynolds-averaged equations for conservation of mass and momentum may be written as follows:

$$\text{Continuity}: \quad \frac{\partial \mathbf{u}}{\partial \mathbf{x}} = 0 \tag{1}$$

$$\text{Momentum}: \quad \frac{\partial}{\partial \mathbf{x}}\left[\mathbf{uu} - (\nu + \nu_t)\frac{\partial \mathbf{u}}{\partial \mathbf{x}}\right] = -\frac{1}{\rho}\frac{\partial p}{\partial \mathbf{x}} + \frac{\partial}{\partial \mathbf{x}}\left[\nu_t \frac{\partial \mathbf{u}}{\partial \mathbf{x}}\right] \tag{2}$$

where **u** is the velocity component in **x**-direction, p is pressure, v is kinematic viscosity, and v_t is the eddy viscosity obtained from the turbulence model.

Among several variations of widely used two-equation turbulence models, the low Reynolds-number (near-wall) version of the k–ω model of Wilcox (1998) is adopted to properly resolve the complex flow behind around the ribs, following the work of Patel and Yoon (1995). This particular model is chosen because of its proven robustness and unambiguous near-wall treatment, two essential attributes in numerical modeling of separated flow about distributed ribs. The eddy viscosity is determined from two transport equations:

Turbulence kinetic energy (k):

$$\frac{\partial}{\partial \mathbf{x}}\left[\mathbf{u}k - \left(v + \frac{v_t}{2}\right)\frac{\partial k}{\partial \mathbf{x}}\right] = P_k - \beta^* k\omega \tag{3}$$

$$Re_\tau = \frac{k}{\omega v}, \quad \beta^* = \frac{9}{100}\cdot\frac{4/15 + (Re_\tau/R_\beta)^4}{1 + Re_\tau/R_\beta}, \quad R_\beta = 8.0$$

Specific dissipation rate (ω):

$$\frac{\partial}{\partial \mathbf{x}}\left[\mathbf{u}\omega - \left(v + \frac{v_t}{2}\right)\frac{\partial \omega}{\partial \mathbf{x}}\right] = \alpha\frac{\omega}{k}P_k - \beta\omega^2 \tag{4}$$

$$\alpha^* = \frac{3/125 + Re_\tau/R_k}{1 + Re_\tau/R_k}, \quad R_k = 6.0$$

$$\alpha = \frac{13}{25}\cdot\frac{1/9 + Re_\tau/R_\omega}{1 + Re_\tau/R_\omega}\frac{1}{\alpha^*}, \quad R_\omega = 2.95, \quad \beta = \frac{9}{125}$$

$$P_k = v_t\left(\frac{\partial u_i}{\partial x_j} + \frac{\partial u_j}{\partial x_i}\right)\frac{\partial u_i}{\partial x_j}$$

where P_k is the production of turbulence kinetic energy, and the eddy viscosity is related to k and ω as

$$v_t = \alpha^*\frac{k}{\omega} \tag{5}$$

2.2. Computational domain and boundary conditions

The no-slip condition is applied on the upper and lower walls of the channel (Figs. 1 and 10). For developed flow in a long channel with regularly spaced roughness elements, the flow is periodic in the streamwise direction. Then it suffices to consider a limited solution domain and impose periodic conditions at the upstream and downstream boundaries. For a channel with three-dimensional roughness, plane-of-symmetry conditions are applied at appropriately located spanwise boundaries. The specific dissipation rate, ω is specified at the first grid off the solid surface and given a value $\frac{6v}{(9\Delta n^2/125)}$, where Δn denotes the normal distance from the wall (Wilcox, 1998). More details on channel geometry, grid and flow conditions are given in later sections.

2.3. Numerical solution procedure

The above equations are solved by a finite-volume method in a non-orthogonal body-fitted colocated grid.

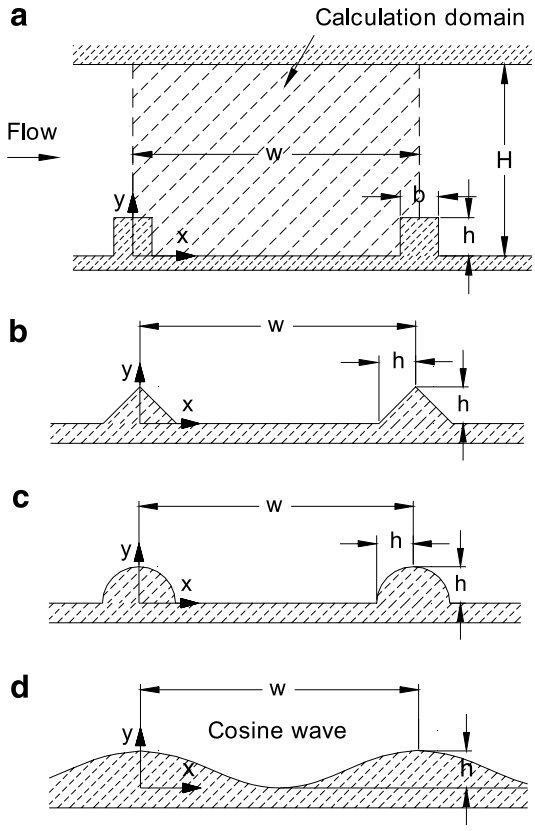

Fig. 1. Schematic of two-dimensional rib-roughened channels and computational domain: (a) square rib; (b) triangular rib; (c) semicircular rib; (d) wavy wall.

Second-order accuracy is assured by adopting the central differencing scheme throughout except for the convective derivatives that are discretized by the QUICK scheme of Hayase et al. (1992). The continuity and the momentum equations, and the model equations for k and ω, are solved iteratively until convergence. The convergence criterion imposed in the calculation is that the sum of the residuals of mass source be less than 10^{-10}.

2.4. Validation tests

The major difficulty of model validation in the present case is the lack of adequately detailed experimental data for various rib shapes and block arrangements. In view of this, model validation is focused on two important features of the analysis: computation of separated flow and implementation of a non-orthogonal grid system. The numerical model outlined above is validated against three test cases, namely, the backward facing step flow, the flow over a wavy wall, and the square-ribbed channel flow, for which previous calculations provide a basis for comparison. Other researchers have also used these cases to validate their solution procedures and turbulence models. Therefore, it suffices to provide a very brief description of the results.

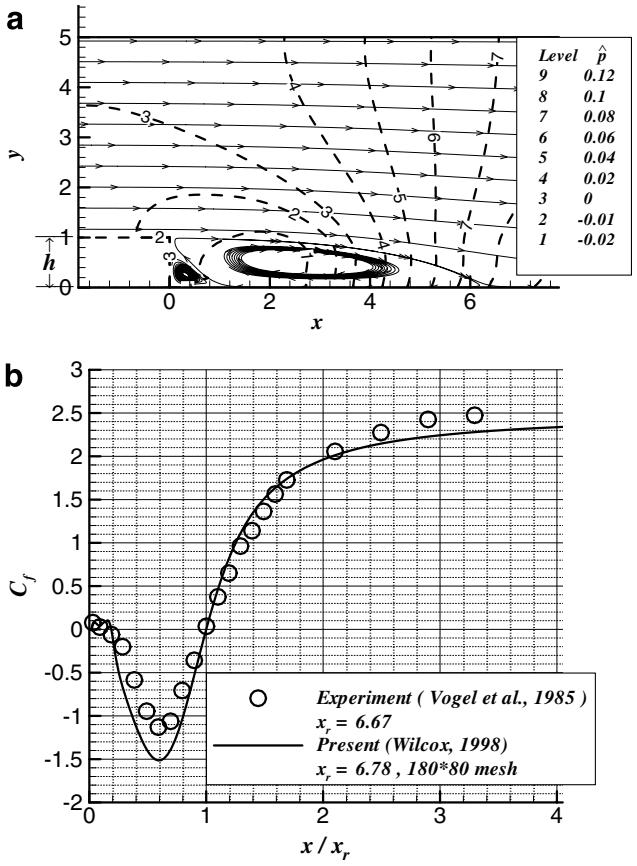

Fig. 2. Backward facing step flow for $Re_h = 28,000$ and $\delta_b/h = 1.1$ at $x/h = -3.8$: (a) streamlines and pressure contours; (b) C_f distribution along the channel.

For the backward facing step flow, calculations were performed in a solution domain $-3.8 < x/h < 80$ with a grid 180×80, in which 30 of the 80 grid points are distributed in the expanded region, for a Reynolds number (Re_h), based on step height h and the mean inlet velocity, of 28,000. The inlet velocity profile is constructed to match the turbulent boundary layer of the experiment, i.e., $\delta/h = 1.1$. Fig. 2 shows the overall flow field and the friction coefficient along the wall downstream of the step. There is good agreement with the measurements of Vogel and Eaton (1985). The computed reattachment length of $6.78h$ also matches well with the experimental value of $6.67h$. These results provide a degree of validation of the numerical method and turbulence model.

The second test case is that of the flow in a channel with a wavy bottom wall and a flat top wall. This flow is chosen primarily to validate the numerical model when used with a generalized non-orthogonal coordinate system. Fig. 3(a) shows the computation domain that extends over one wavelength in the streamwise direction. Periodic conditions are imposed at the upstream and downstream boundaries of the domain. No-slip conditions are applied at the top and bottom walls. The wave amplitude ($2a$) to wavelength (λ) ratio is 0.2, and the Reynolds number based on the hydraulic diameter ($2H$) of the channel is 48,000. Fig. 3(b) and (c) shows the distributions of the friction and pressure coefficients on the wavy wall, respectively. Calculations were made with three meshes, namely, 80×60, 100×80 and 120×100. It is found that the 100×80 mesh is sufficiently fine to resolve the flow field. The present results are compared with the measurements of Buckles et al. (1984) and the LES calculations of Henn and Sykes (1999). The agreement with the pressure and friction data deteriorates near the reattachment point, but the present calculations are found to be in agreement with LES with respect to the friction distribution.

Finally, the flow over the regularly distributed square ribs with $h/D_e = 0.1$ and $w/h = 7.2$, where D_e is the hydraulic diameter, is examined for $Re_{D_e} = 37,200$. The mean velocity profiles at various cross-sections plotted in Fig. 4 are seen to be in good agreement with the measured data of Drain and Martin (1985). The level of agreement is as good as any model, including more sophisticated ones, compared at the reference URL. The discrepancy observed near the top surface of the rib, where the mean velocity attains a local maximum, was first suspected to be due to the insufficient grid resolution (100×80). An additional calculation with much finer grid (160×150) confirms that the solution is indeed grid-independent. Interestingly, all turbulence models compared at the URL fail to accurately capture this behavior. The two-layer model of Chen and Patel (1988) may be the only exception that qualitatively shows the local maximum in the mean velocity in that region. The results of the standard k–ε model with the wall function are shown in the figure for reference.

3. Results and discussion

3.1. Flow over two-dimensional ribs

Spanwise ribs of three shapes, square, triangular, and semicircular, are considered, and a wavy wall with the same height as ribs is included for comparison. They are mounted on the bottom wall of a two-dimensional channel as shown in Fig. 1. Calculations are carried out for a range of Reynolds numbers and rib spacing or pitch (w). The rib height is held constant at $h/D_e = 0.1$, where D_e is the hydraulic diameter of the duct ($= 2H$), i.e., the rib height h is 20% of the channel height, although there is no special difficulty about performing calculations for other heights.

Fig. 5 shows the streamlines and isobars of the representative cases for $Re_{D_e} = 20,000$ and $w/h = 10$. The recirculation zones are clearly identified and the flow is seen to reattach before the following rib (or wave) in all cases. Of the four cases, the flow over the square rib appears to be the most complex; since the rib face is perpendicular to the flow direction, sizable primary and secondary recirculation regions form near the front and rear corners at the rib bottom. The size of the recirculation zone, however, is largest for the triangular rib and smallest for the wavy wall.

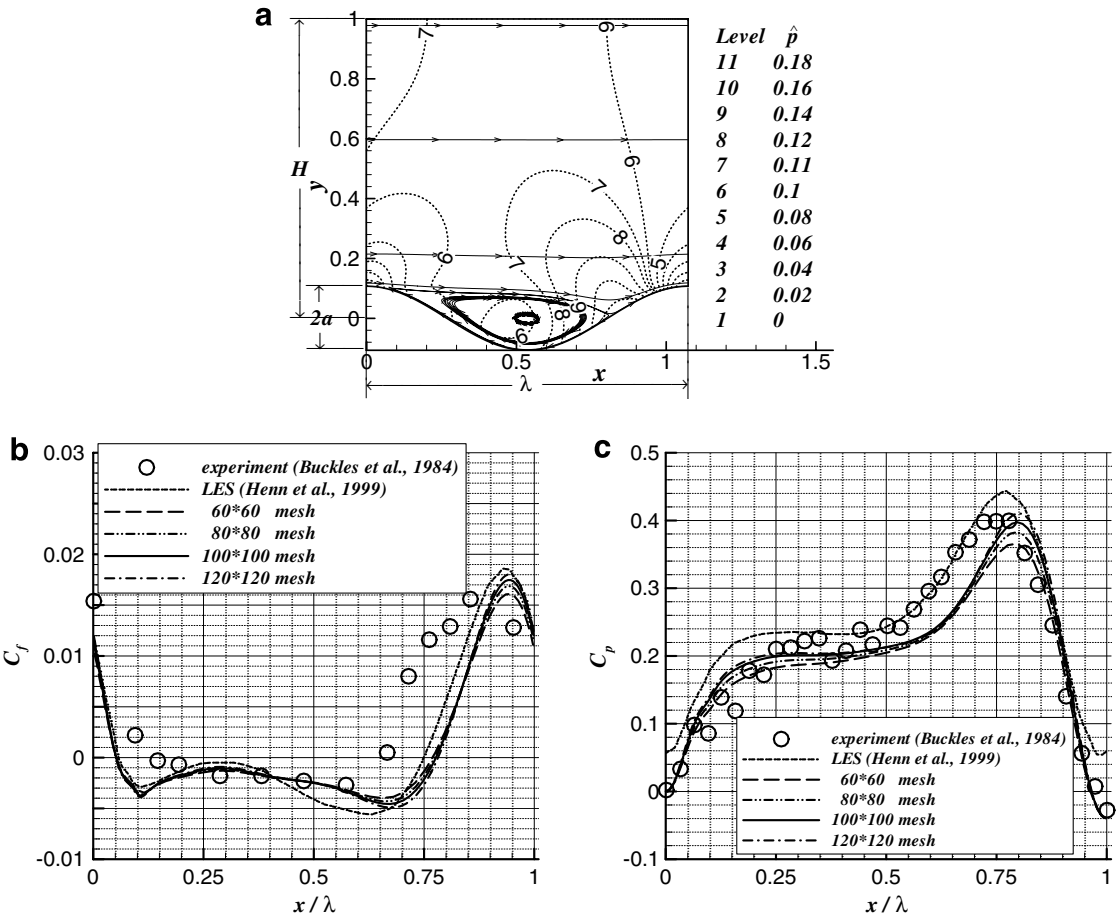

Fig. 3. Wavy wall flow for $2a/\lambda = 0.2$ at $Re_{D_e} = 48,000$: (a) streamlines and pressure contours; (b) skin-friction coefficient; (c) wall pressure distribution.

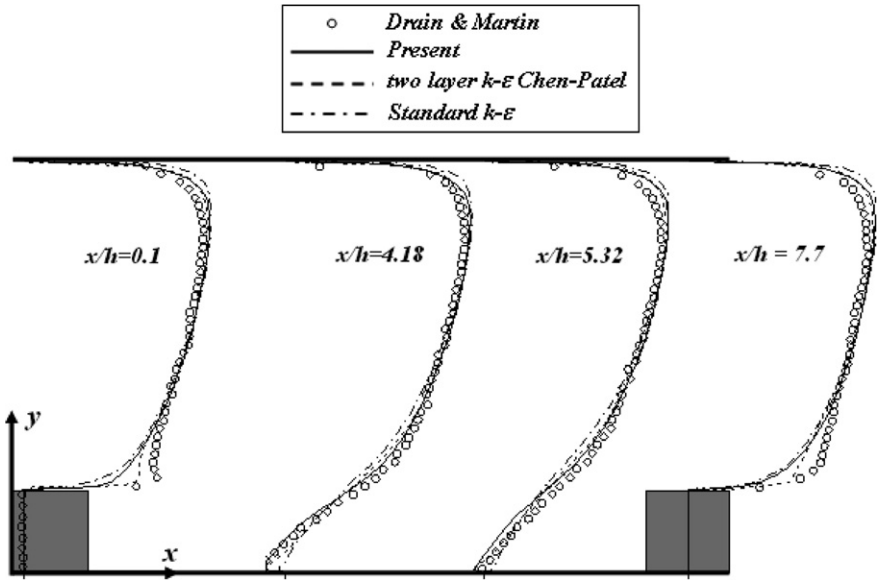

Fig. 4. Mean velocity profiles at various cross-stations for square-ribbed channel with $h/D_e = 0.1$ and $w/h = 7.2$ at $Re_{D_e} = 37,200$.

It is interesting to note that the flow becomes nearly parallel for $y \geqslant 4h$.

The total resistance or effective friction on the rib-roughened surface is made up of pressure and skin-friction forces, and is obtained by surface integration over one pitch (from one rib to the next):

$$\tau_x = \frac{1}{w}\left[\int_S (p_w - p_{ref})\vec{n}\cdot\hat{i}\,ds + \int_S \tau_w \vec{s}\cdot\hat{i}\,ds\right] \quad (6)$$

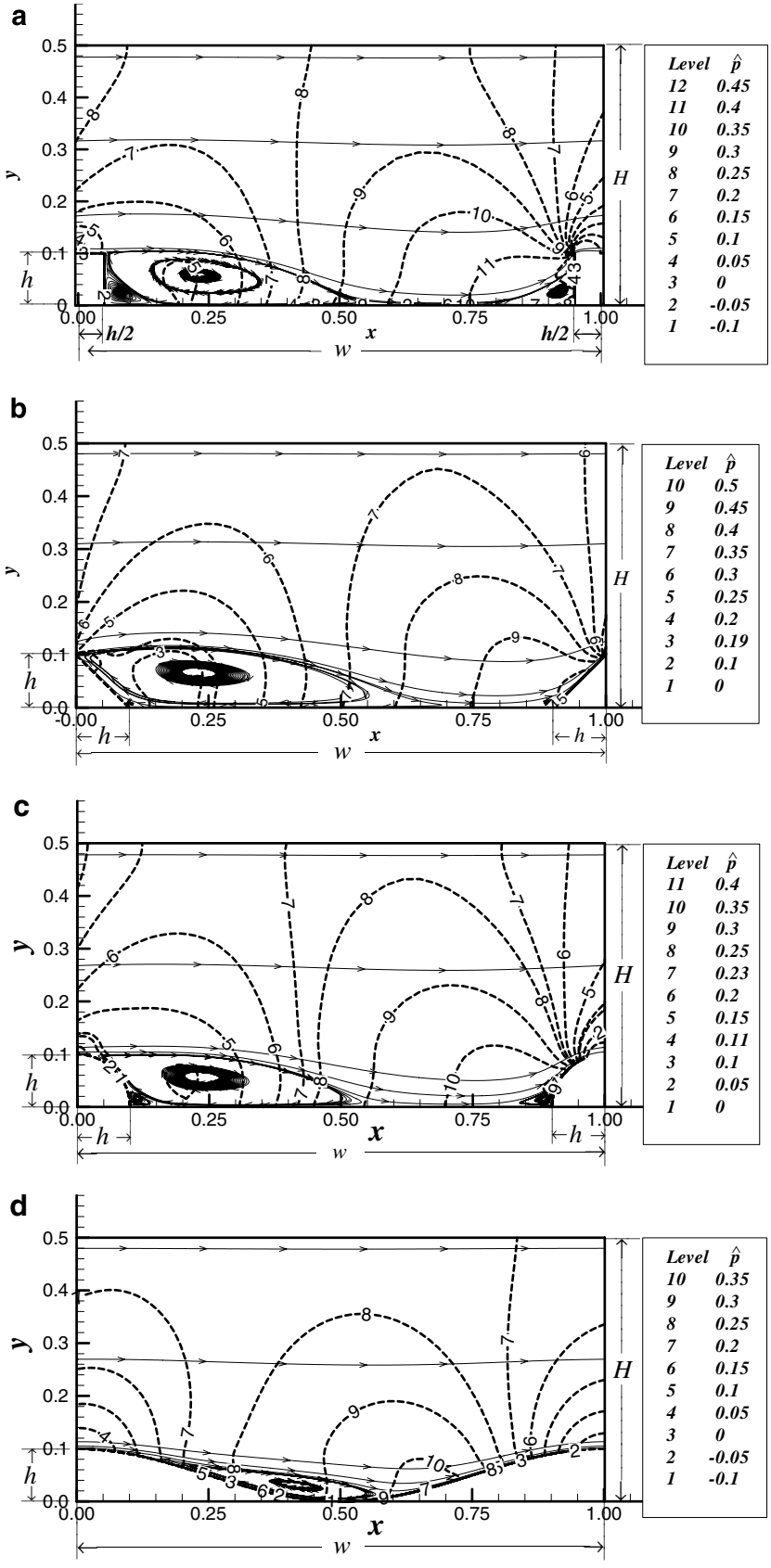

Fig. 5. Streamlines and pressure field for $w/h = 10$ and $h/D_e = 0.1$ at $Re_{D_e} = 20,000$: (a) square rib; (b) triangular rib; (c) semicircular rib; (d) wavy wall.

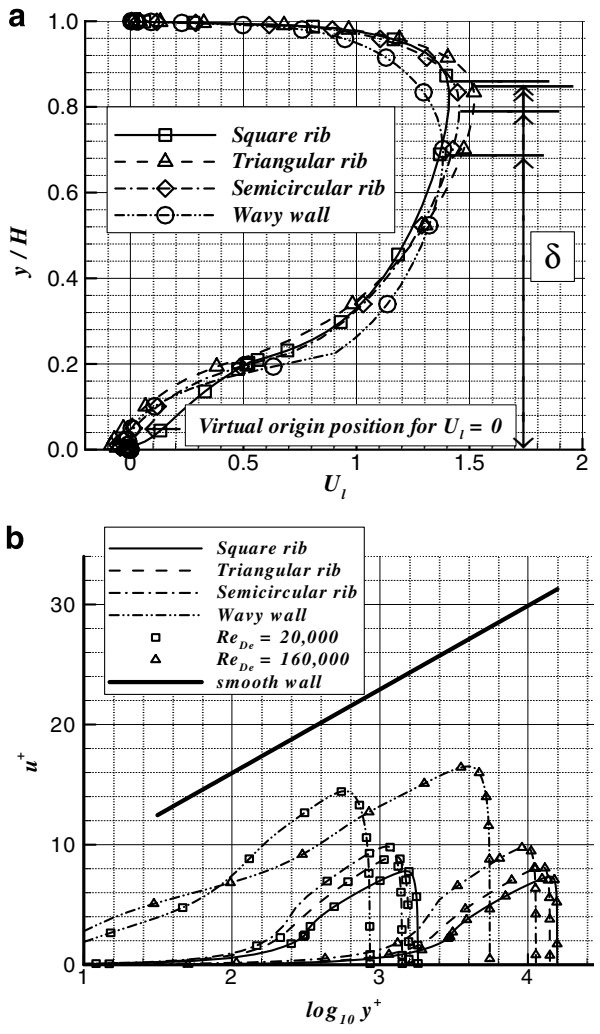

Fig. 6. Mean streamwise velocity profiles for various rib shapes and Reynolds numbers for $w/h = 10$ and $h/D_e = 0.1$: (a) physical coordinates ($Re_{D_e} = 20,000$); (b) wall coordinates.

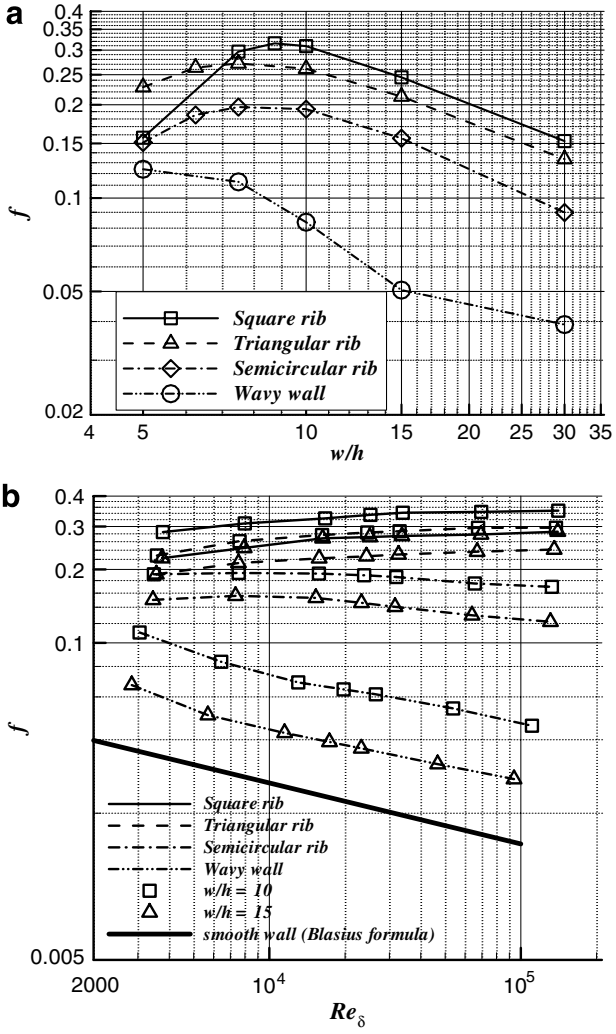

Fig. 7. Mean–resistance factor for various rib shapes for $h/D_e = 0.1$: (a) vs. pitch for $Re_{D_e} = 20,000$; (b) vs. Reynolds number.

where $\vec{n}$, $\vec{s}$ are unit surface normal and tangent vectors, respectively, while $\hat{i}$ denotes the unit vector in the x-direction. The Darcy friction factor f and the friction velocity u_τ are then defined by

$$f = \frac{8\tau_x}{\rho \overline{U}^2}; \quad u_\tau = \sqrt{\tau_x/\rho} \tag{7}$$

where $\overline{U}$ is the average velocity obtained by integration of the velocity profile from the lower wall to the velocity maximum at $y = \delta$ (see Fig. 6), which depends on the roughness and the Reynolds number. The friction velocity defined above is used to plot the velocity profiles in wall coordinates and explore the existence of the logarithmic layer.

For rough surfaces, the logarithmic velocity profile in the wall region differs from that on a smooth surface, and takes the following form:

$$u^+ = \frac{1}{\kappa}\ln(y^+) + B - \Delta B \tag{8}$$

where κ (= 0.418) is the von Karman constant, B is the smooth-wall constant (= 5.45, Patel, 1965), and ΔB the roughness function, which increases with roughness size. The distance y^+ in Eq. (8) is measured from the so-called virtual origin y_0 of the wall, which also increases with increasing roughness. Eq. (8) may be rewritten as

$$u^+ = \frac{1}{\kappa}\ln\left(\frac{y - y_0}{h}\right) + R^+ \tag{9}$$

where

$$R^+ = \frac{1}{\kappa}\ln\left(\frac{hu_\tau}{\nu}\right) + B - \Delta B \tag{10}$$

Eq. (9) is valid for all types of roughness such as ribs, uniform sand, rivets, threads, etc. For sufficiently large roughness, in the so-called fully rough regime, R^+ is constant and assumes the value of 8.5 for sand-grain roughness (Nikuradse, 1950).

Fig. 6 shows the space-averaged streamwise velocity profiles in physical and wall coordinates for various rib shapes. When necessary, a four-point bilinear interpolation is used to obtain the velocity components at desired loca-

tions from those in the generalized computational grids. The virtual origin is identified as the point at which the space-averaged streamwise velocity vanishes and is easily located as shown in Fig. 6(a). From the velocity profiles, it is seen that a large portion (~85%) of the channel is influenced by the lower rough boundary. Except for the wavy-wall case at $Re_{D_e} = 20,000$, the velocity profiles plotted in wall coordinates in Fig. 6(b) clearly exhibit a significant logarithmic region. Also, the logarithmic region begins at higher y^+ and its extent becomes larger when the Reynolds number is increased. It is noted here that the slope of the velocity profile varies slightly across the layer and the logarithmic region is identified as the portion where the slope approximately matches that of the smooth wall. By adjusting the virtual origin, however, the slope can be made to remain fixed at $1/\kappa$. No attempt has been made to fine-tune the virtual origin to recover the exact logarithmic profiles.

The average resistance or friction factor defined in Eq. (7) is plotted in Fig. 7 for various rib shapes for a range of pitch ratio (w/h) and Reynolds number Re_δ ($= \overline{U}\delta/\nu$). For all rib shapes, the resistance initially increases with increasing pitch, reaches a maximum, and gradually decreases toward the smooth wall limit. In general, the resistance is largest for the square rib, and becomes lower as the shape changes to triangular, semicircular, and to a wavy wall. The behavior at lower pitch ratios is somewhat different in the case of square ribs, however. This is because the separation pattern between adjacent ribs is affected to a greater extent as the ribs are more closely spaced. With a pitch ratio of about 4, the square ribs are known to exhibit a *d*-type roughness behavior, as a single eddy is trapped between the adjacent ribs (Perry et al., 1969; Cui et al., 2003a). Then, the pressure on the upstream and downstream faces of the rib is nearly equal and the total resistance is small. Such a behavior has not been reported for ribs of other shapes, although it is possible with sufficiently small pitch ratios.

Fig. 7(b) shows the effect of Reynolds number. It is found that for square and triangular ribs, the resistance increases with Re_δ and soon reaches a plateau, i.e., f becomes independent of Re_δ. The shape of the curve is similar to the well-known Moody diagram for pipes and frictional resistance of rough plates. For semicircular ribs, however, f decreases slowly after reaching a maximum, and in the case of the wavy wall the friction factor

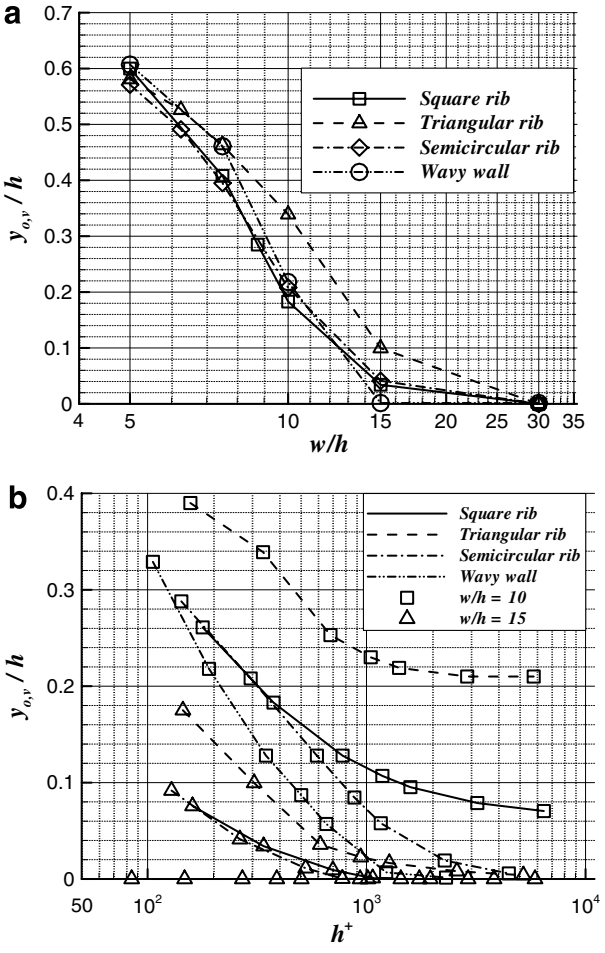

Fig. 8. Location of the virtual origin for various rib shapes for $h/D_e = 0.1$: (a) vs. pitch for $Re_{D_e} = 20,000$; (b) vs. h^+ for two different pitches.

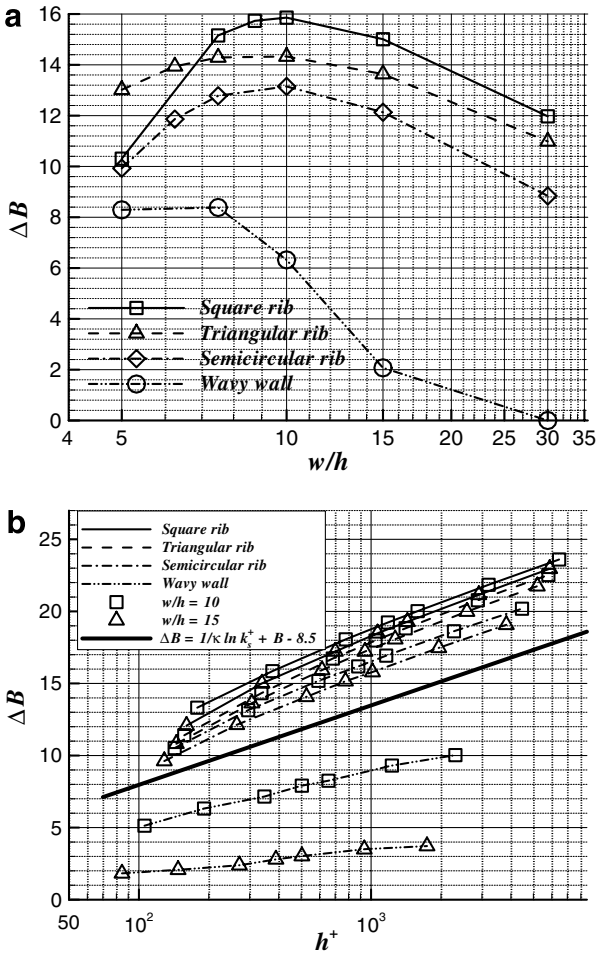

Fig. 9. Roughness function for various rib shapes for $h/D_e = 0.1$: (a) vs. pitch for $Re_{D_e} = 20,000$; (b) vs. h^+ for two different pitches.

decreases as in the case of smooth surfaces, albeit at higher values due to the contribution of pressure resistance. The continuing dependence of friction on Reynolds number in these two cases stems from the movement of the separation and reattachment points on the curved surfaces. It is also seen from Fig. 7(b) that the value of f decreases with increasing pitch ratio w/h but the shape of the curve remains unchanged. Clearly, the results presented in Fig. 7 are of primary interest in design of surfaces for heat transfer enhancement.

Fig. 8 shows the location of the virtual origin defined above as the point above the bottom of the channel where the space-averaged velocity is zero (Fig. 6). While the decrease with the virtual origin with increasing pitch is to be expected, Fig. 8(a) shows that it is relatively insensitive to the shape of the rib when the Reynolds number is fixed. At the lowest pitch ratio of 5, the virtual origin is located $0.6h$ above the channel bottom, or $0.4h$ below the top of the rib. Fig. 8(b) shows that for a given pitch ratio the distance to the virtual origin from the bottom of the channel decreases as the roughness Reynolds number h^+ $(= hu_\tau/\nu)$ increases, and asymptotically approaches some constant value, zero or finite depending on the pitch, for large h^+. In general, it is quite difficult to determine the virtual origin in experiments and uncertainties in its location have clouded discussion about the logarithmic layer, and even determination of the friction factor from velocity measurements over rough surfaces. Numerical solutions such as these are useful to understand the issues that are involved and perhaps quantify the uncertainty in measurements.

An important quantity of interest in rough wall flows is the roughness function ΔB. The computed velocity profiles when plotted in the format of Fig. 6(b) enable determination of the roughness function ΔB for each rib configuration and Reynolds number. The results are plotted in Fig. 9. The variation of this function with pitch is very similar to that of the friction factor in Fig. 7(a) for obvious reasons. However, its variation with the roughness Reynolds number h^+ in Fig. 9(b) is of great interest. It is seen that for all three rib shapes and pitch ratios, ΔB is a logarithmic function of h^+ with a slope of κ^{-1}. The correlation for each case differs by a constant, which varies with the rib shape and pitch

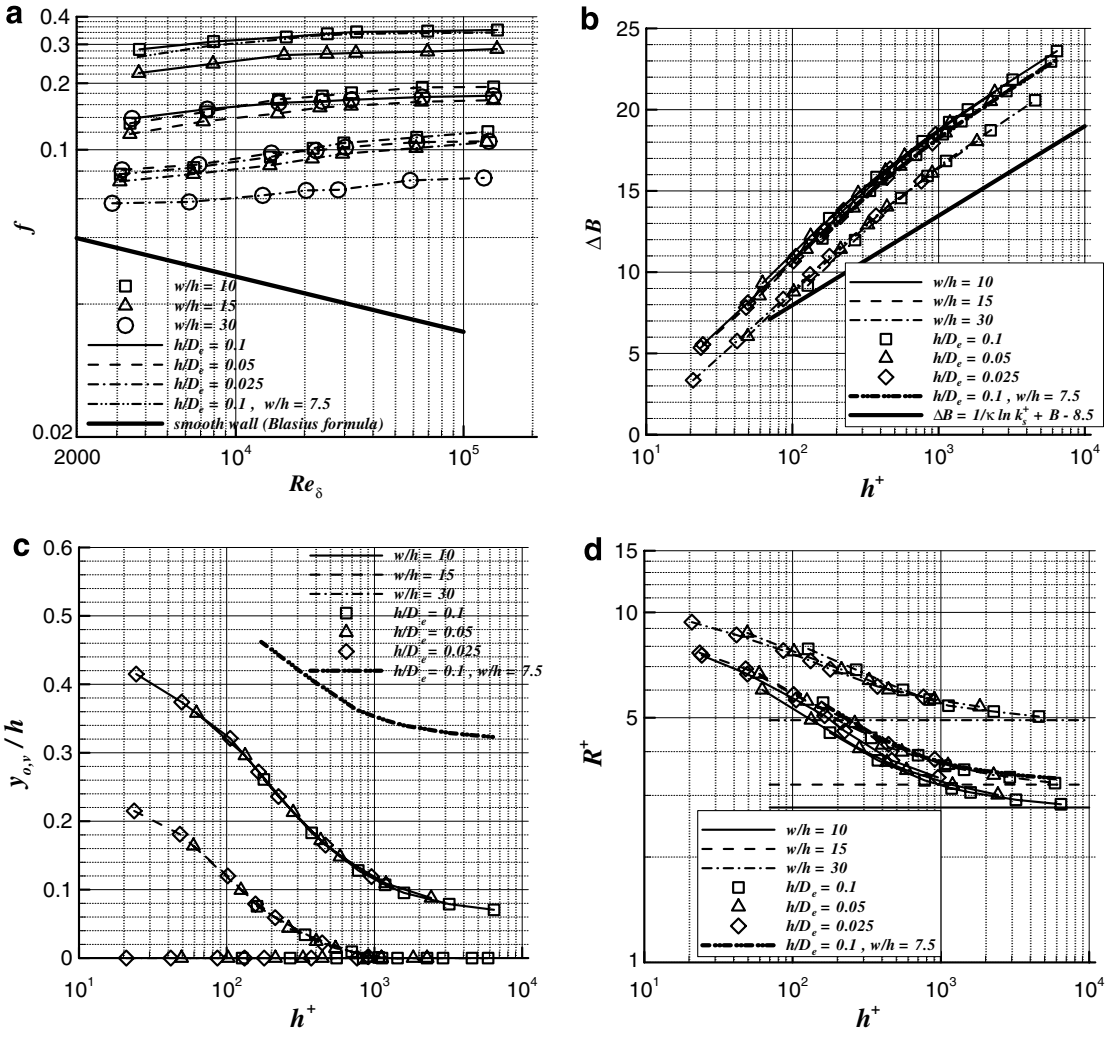

Fig. 10. Flow characteristics for square ribs: (a) friction factor; (b) roughness function; (c) location of virtual origin; (d) roughness correlation.

ratio. The slope for wavy wall deviates considerably from κ^{-1}, especially for the larger pitch and suggests that the wavy wall behaves differently from ordinary roughness. The bold line for classic Prandtl–Schlichting sand-grain roughness is included for reference. This may be used to determine the so-called equivalent sand-grain roughness k_s for different rib arrangements.

To further characterize rib-roughened surfaces, a series of calculations is carried out for square ribs of various sizes (h/D_e) and pitch ratios (w/h). The results are summarized in Fig. 10. Fig. 10(a) shows the effect of rib height and pitch on the friction factor. The magnitude of f decreases with pitch and increases with rib height. The effect of Reynolds number decreases with increasing Reynolds number, and the flow over larger ribs becomes Reynolds-number independent at smaller values.

The roughness function is plotted as a function of roughness Reynolds number in Fig. 10(b). It is interesting to note the collapse of the results for the three values of the rib size relative to the channel hydraulic diameter. This is clear evidence of the fact that the channel height does not influence the flow on the rough wall. In other words, the influence of pitch and Reynolds number are independent of the geometry of the flow selected for the numerical simulations. For each pitch ratio, the roughness function increases with roughness Reynolds number and becomes logarithmic at sufficiently large Reynolds numbers. In each case, the slope recovers κ^{-1} as h^+ becomes sufficiently large, parallel to the correlation for sand-grain roughness. As noted earlier, these results may be used to determine the equivalent sand-grain roughness for each rib arrangement. Fig. 10(c) shows that the position of the virtual origin is also independent of the channel height. The variation with the roughness Reynolds number was discussed above with reference to Fig. 8(b). The roughness correlation R^+ defined in Eq. (10) is shown in Fig. 10(d). For each rib configuration it decreases with increasing Reynolds number before reaching a constant value at sufficiently high Reynolds numbers, but different from the value of 8.5 for uniform sand-grain roughness. Taken together, the results of

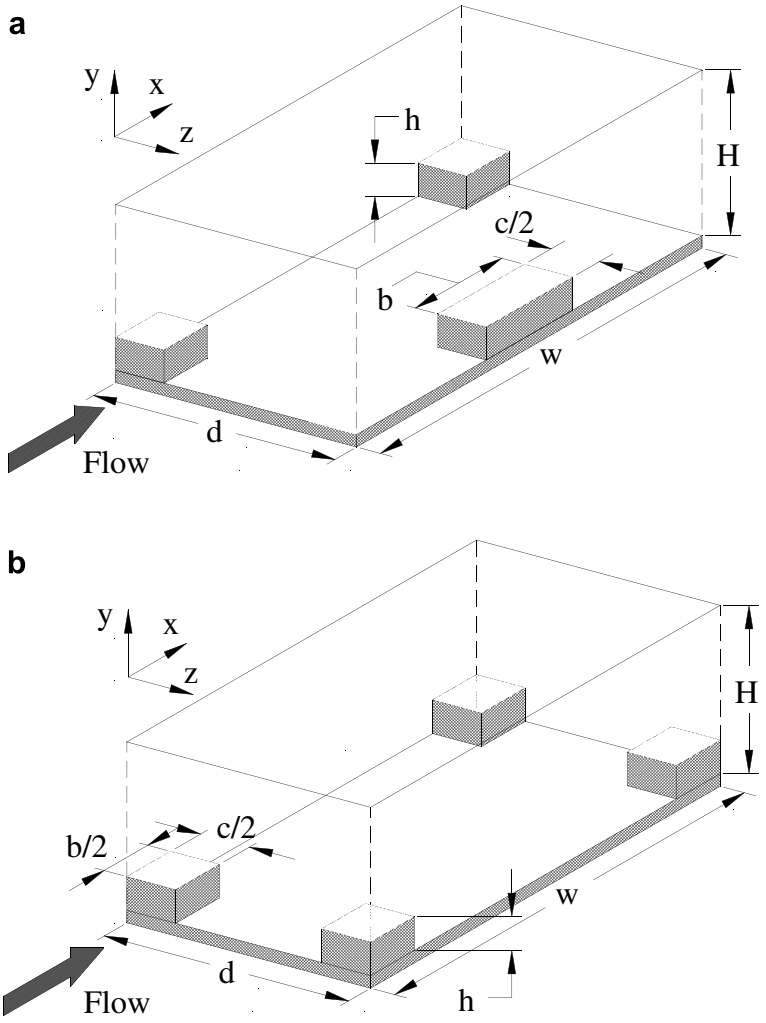

Fig. 11. Schematic of channel with distributed hexahedral blocks ($h = 0.1$, $b = 0.3$, $H = 0.5$, $d = 0.75$ are fixed): (a) staggered distribution; (b) in-line distribution.

Fig. 10 show that the flow becomes fully rough and independent of Reynolds number when h^+ is greater than, say, 5×10^3.

3.2. Flow over three-dimensional roughness elements

The numerical simulations are now extended to three-dimensional flow over uniformly distributed hexahedral blocks. Compared to the two-dimensional cases, there are many more geometric parameters to deal with. For present purposes, however, we examine two representative block cross-sections: a square section and a rectangular section of spanwise aspect ratio of two, in in-line and staggered arrangements, as shown in Fig. 11. The transverse block spacing d/D_e and streamwise length of the block b/D_e are held constant at 0.75 and 0.3, respectively. The block height and pitch (streamwise spacing) are parameters that are varied. For $w/h = 15$ and 18, a non-uniformly distributed grid of $104 \times 64 \times 61$ cells is used while a grid with $80 \times 64 \times 51$ cells is used for $w/h = 6$, 9 and 12.

Typical flow patterns (not shown) exhibit that the flow around the staggered blocks is much more violent than that around the in-line blocks, in which the disturbance appears to be confined to immediate neighborhood of the block. The fluid passes between the distributed blocks in fairly orderly fashion for the in-line arrangement, while that for the staggered arrangement meanders around the obstacles and makes the vortical motion very intense. This is clearly illustrated in the cross-flow pattern of each case in Fig. 12. Fig. 12(a) shows the cross-plane streamlines at $x/D_e = 0.6$ for the staggered rectangular blocks. Two large and strong streamwise vortices span the entire channel. For the other three cases, on the other hand, the vortical motion is not as intense and is confined to the vicinity of the wall. This is true even for the rectangular block if the distribution is in-line and the square blocks in the staggered arrangement.

As is in two-dimensional case, the skin friction and pressure distributions are integrated over appropriate surface areas to calculate the effective total resistance:

$$\tau_x = \frac{1}{wd}\left[\int_{S_x}(p_w - p_{ref})\mathrm{d}S_+ \int_{S_y}\tau_{wx}\,\mathrm{d}S\right] \tag{11}$$

where τ_{wx} is the skin-friction component in the x-direction, S_x denotes the vertical surfaces of the block whose normal is in x-direction, and S_y denotes the floor and horizontal surfaces of the blocks whose normal is in y-direction. The friction factor and friction velocity are then defined as in Eq. (7).

The numerical model was again used to simulate the flow in channels with different block arrangements, varying

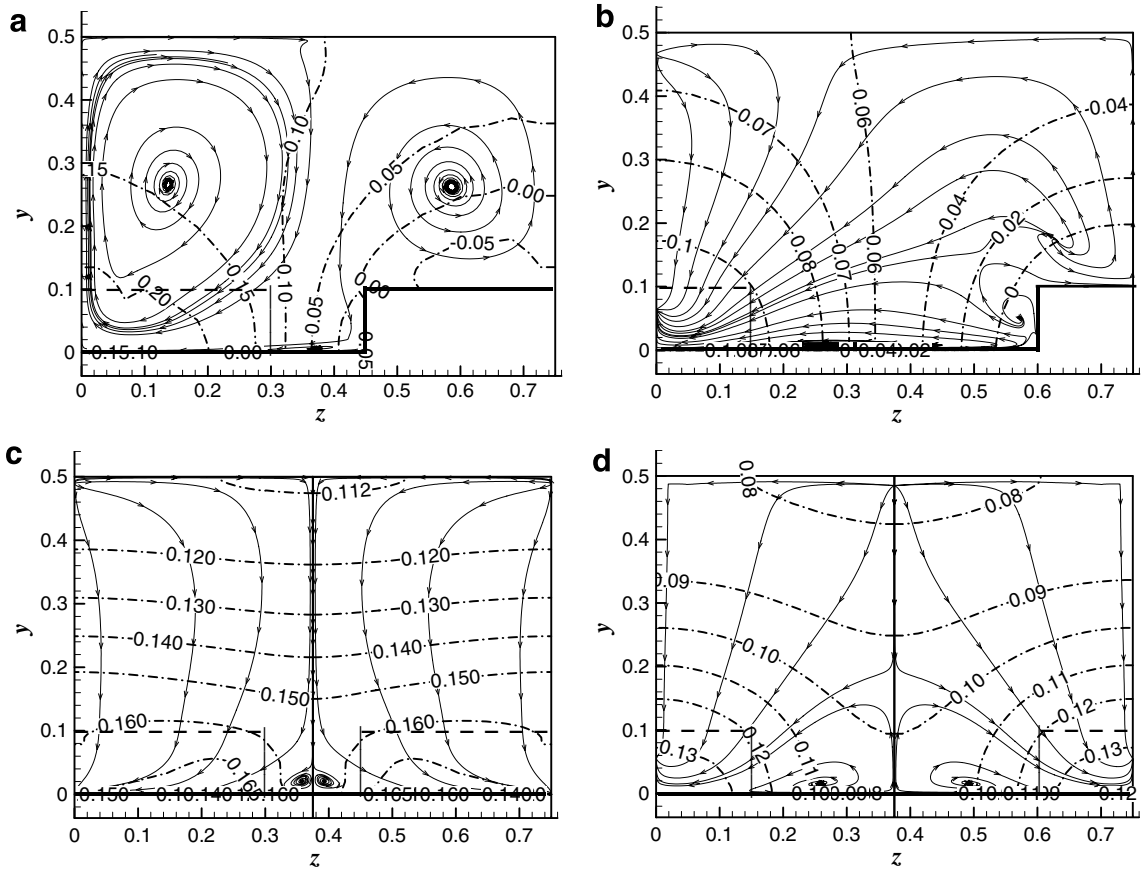

Fig. 12. Cross-flow patterns and pressure ($\hat{p}$) distributions at $x/D_e = 0.6$ for $w/h = 12$, $h/D_e = 0.1$, and $Re_{D_e} = 20,000$: (a) $c = 2b$ (staggered); (b) $c = b$ (staggered); (c) $c = 2b$ (in-line); (d) $c = b$ (in-line).

the block height and the Reynolds number. Fig. 13 shows the space-averaged velocity profiles in wall coordinates for $c = 2b$ for three block heights and two Reynolds numbers. From these and similar plots for other geometries it is found that, in general, the velocity profiles have logarithmic regions for blocks in the in-line arrangement. The logarithmic regions are better defined as the block size is reduced and/or the Reynolds number is increased, as might be expected from the extent of the disturbance introduced by the blocks. With the staggered blocks, however, the flow is disturbed so much that a well-defined logarithmic region exists only for sufficiently small block heights, typically less than 5% of the channel height. In other words, taller blocks cannot be regarded as roughness in the traditional sense, and consequently, it is not appropriate to use correlations for friction and heat transfer based on the logarithmic velocity profile. All profiles for rectangular blocks in in-line arrangement and for square blocks in either arrangement (not shown) contain a logarithmic region.

As in the case of two-dimensional ribs, the resistance coefficients and roughness functions for $h/D_e = 0.1$ are shown in Figs. 14 and 15, respectively. Some values of ΔB for this block height are estimated, as the logarithmic region could not be clearly identified for some block arrangements. The results for two-dimensional ribs of the same relative height and length to height ratio are also shown for comparison. It is seen that the friction factor and the roughness function attain maximum values somewhere between $w/h = 10$ and 15, which is very similar to two-dimensional cases. The block spacing that results in maximum drag is often associated with the point of maximum heat transfer, which is the subject of *Part II* of this paper. It is interesting to observe that the resistance for blocks of square cross-section is comparatively small and identical for both block arrangements while that for the rectangular block is larger and there is substantial difference between the in-line and staggered arrangements. For the rectangular blocks, the in-line arrangement gives a smaller resistance, even smaller than the two-dimensional

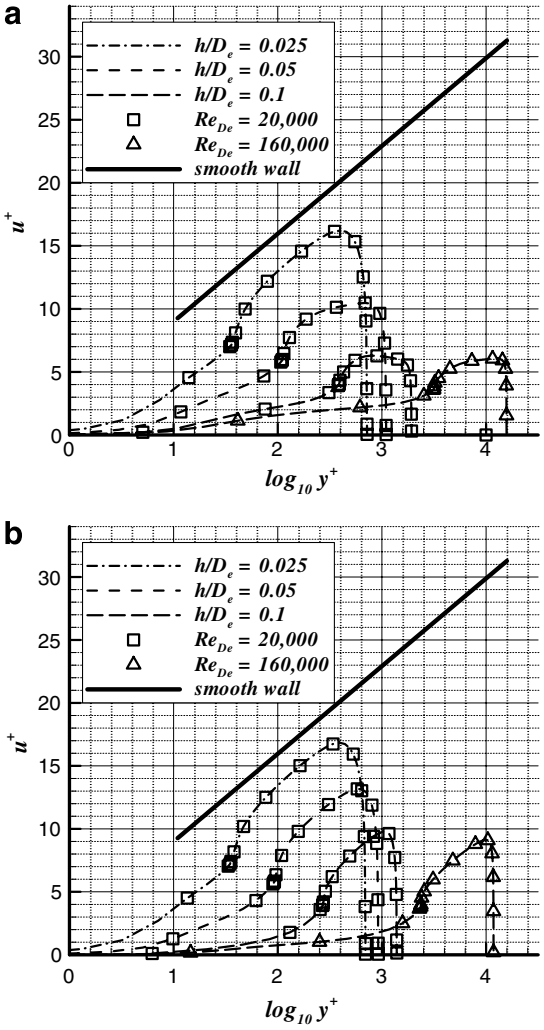

Fig. 13. Mean streamwise velocity profiles in wall coordinates for $w/h = 12$ and $c = 2b$ with various block heights: (a) staggered arrangement; (b) in-line arrangement.

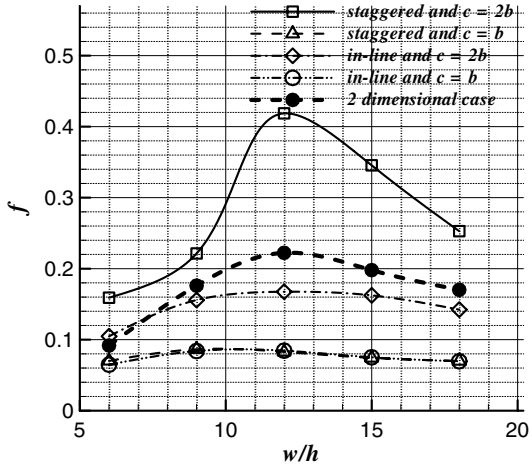

Fig. 14. Friction factor vs. pitch for $h/D_e = 0.1$ at $Re_{D_e} = 20,000$.

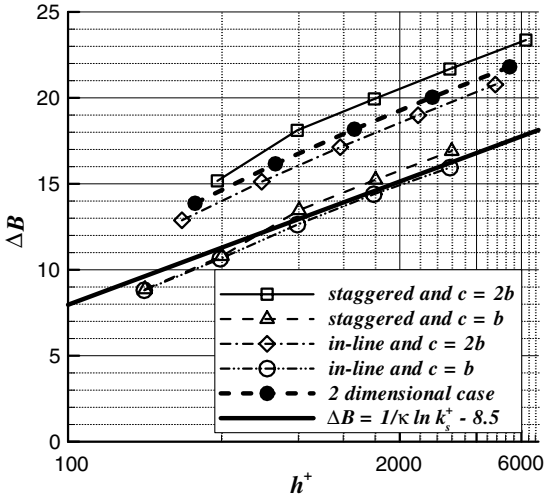

Fig. 15. Roughness function vs. pitch for $h/D_e = 0.1$ at $Re_{D_e} = 20,000$.

ribs, while the staggered arrangement exerts much larger resistance on the flow than the two-dimensional ribs. This is due to the fact that the fluid has to turn more wildly to go around the staggered blocks and, hence, creates a much greater disturbance in the outer flow when the block is tall. This was confirmed by additional calculations with smaller blocks. As in two-dimensional cases, the roughness function ΔB varies logarithmically with slope $1/\kappa$ with increasing h^+.

4. Conclusions

The most important conclusion drawn from this research is that a numerical model based on the Reynolds-averaged Navier–Stokes equations coupled with a turbulence model that resolves the near-wall flow is able to successfully capture the essential features of the flow over the surface with two-dimensional ribs and three-dimensional blocks. When the solutions are averaged over appropriate areas, they provide engineering information about the resistance coefficient and its dependence on the geometric and flow parameters. In addition, the numerical model provides details of the velocity profile, such as the roughness function and the virtual origin, that have hitherto fore been the purview of experimental correlations, and information about the flow in the roughness layer, within the interstices of the roughness elements, that is difficult to measure and quantify by experiments. Although the latter aspects of the solutions have not been examined in any detail in the present paper, they are of interest in understanding the interaction between the spatially non-uniform flow in the roughness layer and the outer flow that feels only an averaged effect of a rough wall. Previous experience with contemporary turbulence models suggests that use of alternate models will confirm the principal results of this study.

The flow over two-dimensional ribs of different shapes is studied to examine the resistance coefficient as well as the velocity profiles. It is found that square ribs exert the most resistance among the four shapes considered while the wavy wall offers the least. Maximum resistance occurs at the pitch to height ratio below 10. The space-averaged velocity profile shows a logarithmic region for ribs as large as 20% of the channel height. For three-dimensional flows, the logarithmic region exists for blocks of much smaller heights, typically less than 5% of the channel height. Thus, the flow over larger blocks cannot be treated within the traditional framework of surface roughness that is based on the assumption of a logarithmic layer. Of course, this does not diminish the usefulness of the numerical model. On the contrary, a numerical model provides information that cannot be obtained by extrapolation of existing roughness correlations.

The roughness function for two-dimensional flow is found to vary linearly with the log of the roughness Reynolds number h^+. The slope reaches the value of κ^{-1} for sufficiently large h^+, confirming the trends established by experiment for other types of roughness. Regardless of the rib size, the results collapse on to a single curve if the pitch is kept constant. For three-dimensional blocks, the resistance and the roughness function depend on the block shape and arrangement.

The numerical model is extended to study heat transfer (Ryu et al., in press) in channels with two-dimensional ribs and three-dimensional blocks. It is found that the logarithmic region also exists in the space-averaged temperature profile if the velocity distribution has a logarithmic layer.

Acknowledgements

This work was supported by KISTEP under Grant 2-578 through the National Research Lab. Program and, in part, by KOSEF through Combustion Engineering Research Center. The authors thank IIHR – Hydroscience and Engineering, The University of Iowa, for support of this collaborative research. Referees' useful comments that helped ameliorate the paper are also greatly appreciated.

References

Buckles, J., Hanratty, T.J., Adrian, R.J., 1984. Turbulent flow over large amplitude wavy surface. J. Fluid Mech. 140, 27–44.

Chen, H.C., Patel, V.C., 1988. Near-wall turbulence models for complex flows including separation. AIAA J. 26, 641–648.

Cui, J., Patel, V.C., Lin, C.L., 2003a. Large-eddy simulation of turbulent flow in a channel with rib roughness. Int. J. Heat Fluid Flow 24, 372–388.

Cui, J., Lin, C.L., Patel, V.C., 2003b. Use of large-eddy simulation to characterize roughness effect of turbulent flow over a wavy wall. ASME J. Fluids Eng. 125, 1075–1077.

Drain, L.E., Martin, S., 1985. Two-component velocity measurements of turbulent flow in a ribbed-wall flow channel. In: International Conference on Laser Anemometry – Advances and Applications, Manchester, UK. <http://tmdb.ws.tn.tudelft.nl/workshop7/case7_2/case72d.html>.

Dvorak, F.A., 1969. Calculation of turbulent boundary layers on rough surfaces in pressure gradient. AIAA J. 7, 1752–1759.

Hayase, T., Humphrey, J.A.C., Grief, R., 1992. A consistently formulated QUICK scheme for fast and stable convergence using finite-volume iterative calculation procedure. J. Comput. Phys. 98, 108–118.

Henn, D.S., Sykes, R.I., 1999. Large-eddy simulation of flow over wavy surface. J. Fluid Mech. 383, 75–112.

Ikeda, T., Durbin, P.A., 2002. Direct simulations of a rough-wall channel flow. Stanford Univ. Mech. Eng. Report No. TF-81.

Jimenez, J., 2004. Turbulent flow over rough walls. Ann. Rev. Fluid Mech. 36, 173–196.

Miyake, Y., Tsujimoto, K., Nagai, N., 2002. Numerical simulation of channel flow with a rib-roughened wall. J. Turbulence 3, 1–17.

Nikuradse, J., 1950. Laws for flow in rough pipes. NACA TM, 1292.

Patel, V.C., 1965. Calibration of the Preston tube and limitations on its use in pressure gradient. J. Fluid Mech. 23, 185–208.

Patel, V.C., Yoon, J.Y., 1995. Application of turbulence models to separated flow over rough surfaces. ASME J. Fluids Eng. 117, 234–241.

Perry, A.E., Schofield, W.H., Joubert, P.N., 1969. Rough wall turbulent boundary layers. J. Fluid Mech. 37, 383–413.

Ryu, D.N., Choi, D.H., Patel, V.C., in press. Analysis of turbulent flow in channels roughened by two-dimensional ribs and three-dimensional blocks. Part II: heat Transfer. Int. J. Heat Fluid Flow, doi:10.1016/j.ijheatfluidflow.2006.11.007.

Schlichting, H., 1979. Boundary-Layer Theory, seventh ed. McGraw Hill, pp. 598–634.

Sparrow, E.M., Tao, W.Q., 1983. Enhanced heat transfer in a flat rectangular duct with streamwise-periodic disturbances at one principal wall. Trans. ASME J. Heat Trans. 105, 851–861.

Vogel, J.C., Eaton, J.K., 1985. Combined heat transfer and fluid dynamic measurements downstream of a backward-facing step. Trans. ASME J. Heat Transfer 107, 922–929.

Webb, R.L., Eckert, E.R.G., Goldstein, R.J., 1971. Heat transfer and friction in tubes with repeated-rib roughness. Int. J. Heat Mass Transfer 14, 601–617.

Wilcox, D.C., 1998. Turbulence Modeling for CFD, second ed. DCW Industries.